Refractive Index Sensing Using Small-Period LPGs in Transmission and Reflection Configurations

R. Funari, R. M. A. Ayaz, F. Di Pasquale, and C. J. Oton

***Abstract*—Long-period gratings (LPGs) are promising photonic chemical sensors since they can excite cladding modes that interact with the surrounding medium. Small-period long-period gratings (SP-LPGs) allow the excitation of higher-order cladding modes, providing enhanced sensitivity and improved noise performance compared to conventional LPGs. In this work, we present both simulation and experimental results on refractive index sensing using SP-LPGs, specifically comparing their operation in transmission and reflection configurations. We experimentally demonstrate that the two configurations exhibit comparable performance in terms of sensitivity and noise, thus offering flexibility for sensing applications where access to both fiber ends is limited. The experimental results show an excellent agreement with simulations, highlighting the robustness and versatility of SP-LPG-based sensors.**

***Index Terms*—Fiber optic sensors, long period grating, LPG, refractive index sensing, small-period long period grating, SP-LPG, femtosecond laser written LPG, transmission, reflection.**

I. Introduction

FIBER optic sensors have become a key technology in modern sensing applications owing to their inherent advantages, including high sensitivity, immunity to electromagnetic interference, and suitability for remote operation [1], [2], [3], [4]. Among the various architectures, Fiber Bragg Gratings (FBGs) [5] and Long Period Gratings (LPGs) [6], [7] are particularly noteworthy due to their unique working principles and versatility across multiple application domains. Both types of gratings are typically realized by inscribing periodic perturbations in the refractive index (RI) of the fiber core.

Standard FBG [4], [5] typically operate in first-order reflection mode, with a grating period of $\Lambda \approx 530$ nm for the 1550 nm wavelength range. In such gratings, light remains confined within the core, making these sensors responsive only to parameters that affect the core region, such as temperature or strain, while being mostly insensitive to external RI variations. To achieve sensitivity to the surrounding environment, the cladding must be modified, either by reducing its thickness through tapering or side-lapping [8], or by designing the grating to couple light into cladding modes. In these modes, part of the light propagates near the cladding surface, where it can interact with the surrounding medium. Cladding mode excitation can be achieved by adjusting the grating period, allowing coupling to occur in either co-propagating or counter-propagating configurations [9], [10]. In counter-propagating schemes, the spectral spacing between cladding mode resonances is typically very small, making individual peaks difficult to resolve and track. In contrast, co-propagating configurations provide well-separated cladding mode resonances and require longer grating periods, ranging from 12 μm to 1 mm for water-surrounded cladding [11]. Gratings with such extended periods are classified as Long Period Gratings (LPGs). LPGs exhibit dips in their transmission spectrum, each corresponding to a specific cladding mode or a family of cladding modes. Changes in the surrounding RI cause these resonances shift due to the interaction between the evanescent field of the cladding modes and the surrounding medium. Monitoring these shifts enables accurate RI sensing, which can be further enhanced by surface functionalization for chemical or biological selectivity.

Over the years, LPGs have been extensively investigated for the measurement of temperature [12], [13], strain [14], [15], bending [16], [17], and torsion [18], with particular emphasis on surrounding RI [19], [20], [21]. As a result, LPGs have found broad applicability in physical [22], [23], chemical [24], and biological [2], [25], [26], [27] sensing domains. Despite their versatility, LPGs face several limitations. Their cross-sensitivity to temperature and strain often requires careful design to isolate RI responses, and their long grating periods (typically >100 μm) lead to devices several centimeters in length, posing challenges for compact or integrated sensing applications [28], [29].

To address these challenges, small-period long-period gratings (SP-LPGs) [28], [30], [31], [32], [33], also referred to in the literature as high-order-mode LPGs [34], have been developed as a compact alternative to conventional LPGs. Owing to their shorter period (10–50 μm), SP-LPGs require much shorter grating lengths, typically a few millimeters, allowing miniaturization and integration into space-constrained environments. Moreover, shorter periods excite higher-order cladding modes, which have a higher evanescent field in the surrounding

Received 31 July 2025; revised 27 October 2025, 10 December 2025, and 22 December 2025; accepted 8 January 2026. Date of publication 13 January 2026; date of current version 6 April 2026. This work was supported in part by the Department of Excellence in Robotics & AI, in part by Scuola Superiore Sant'Anna, in part by Piazza Martiri della Libertà, Pisa, Italy, in part by Project BRIEF "Biorobotics Research and Innovation Engineering Facilities" (Project identification code IR0000036) funded by National Recovery and Resilience Plan (NRRP), and in part by the Mission 4 Component 2 Investment 3.1 of Italian Ministry of University and Research funded by European Union – NextGenerationEU. *(Corresponding author: R. Funari.)*

The authors are with the Institute of Mechanical Intelligence, Scuola Superiore Sant'Anna, 56124 Pisa, Italy (e-mail: riccardo.funari@santannapisa.it; ranamuhammadarmaghan.ayaz@santannapisa.it; fabrizio.dipasquale@santannapisa.it; c.oton@santannapisa.it).

This article has supplementary material provided by the authors and color versions of one or more figures available at https://doi.org/10.1109/JLT.2026.3653642.

Digital Object Identifier 10.1109/JLT.2026.3653642

medium. As a consequence, the sensitivity to liquid refractive index variations is expected to be higher than for lower-order cladding modes (although this is not always true as sensitivity can also be strongly enhanced by dispersion, as discussed in next section). In Ref. [35], the RI sensing performance of SP-LPGs fabricated with femtosecond laser inscription was investigated, with the 13 μm-period device exhibiting improved sensitivity and reduced noise. That same work also includes a comparison table summarizing the characteristics of conventional LPGs and SP-LPGs, including the 13 μm period grating, providing additional context for the advantages of short-period structures.

In this work, we investigate SP-LPGs with a period of 13 μm and characterize their performance in both transmission and reflection configurations. While transmission mode is more common for LPG devices, since it does not require additional modification of the fiber after the grating is inscribed in the core, operation in reflection mode can be realized by integrating a reflective element beyond the grating, the fiber optic device to function as a single-ended sensor.

A variety of RI sensing technologies have been developed, each with distinct advantages and limitations. Standard FBGs can also be used for RI sensing by etching the cladding of the fiber [36]. However, this approach makes the fiber more fragile and difficult to handle. Mach-Zehnder interferometers (MZIs) provide high sensitivity and phase-based detection [37], yet they typically require complex alignment and interferometric stabilization, which can hinder compact and robust deployment. Non-fiber optic approaches, such as surface plasmon resonance (SPR) [38], localized surface plasmon resonance (LSPR) [39], [40], and silicon photonic sensors [41], [42], can achieve excellent sensitivity and miniaturization, but they often involve expensive fabrication and delicate surface functionalization. In comparison, SP-LPGs combine strong evanescent field interaction with compact geometry, high RI sensitivity, and relatively simple fabrication, making them a versatile and practical solution for both laboratory and field applications.

Fig. 1 depicts both sensing schemes, in transmission and in reflection. In both configurations, only the core mode is detected, which shows decreases of power when cladding modes are excited. Cladding modes are not detected because they are lost in the coated section of the optical fiber. Transmission-mode operation is advantageous in terms of sensor fabrication and is well suited for laboratory or benchtop setups where access to both fiber ends is available. On the other hand, reflection-mode operation enables single-ended connectivity, making it highly suitable for deployment in confined, embedded, or remote environments, such as in vivo diagnostics, environmental monitoring in wells or pipelines, and industrial process control. By demonstrating that both configurations exhibit comparable sensitivity and experimental performances, this study provides valuable insights for selecting the optimal configuration based on application-specific constraints. These findings highlight the potential of SP-LPGs as tunable and versatile sensors, where the choice of grating period and optical configuration allows for optimization according to different operational requirements.

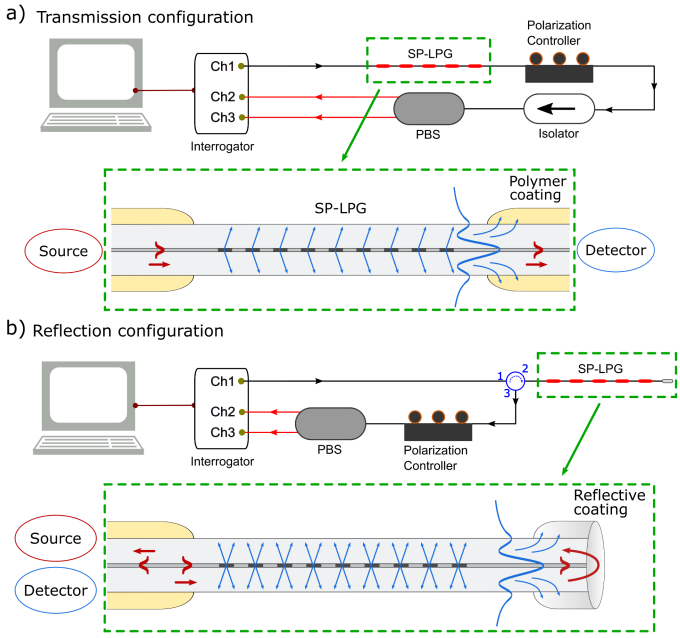

Fig. 1. Schematic representation of the SP-LPG operating in (a) transmission and (b) reflection modes. In SP-LPGs, core-guided light couples into cladding modes at the grating, generating an evanescent field that is sensitive to changes in the surrounding refractive index (RI). In transmission mode, cladding modes get lost in the coating, while in reflection mode, cladding modes are generated in both directions, but get lost in the coated regions in either side.

II. Design and Model

We have modeled the fiber as a three-layer dielectric cylindrical stack which includes a 8.2 μm-radius core, a 125 μm-radius cladding, and surrounding water. The method used is a 4×4 transfer-matrix approach as described in [43], [44]. The EH mode profiles are calculated using python, assuming cylindrical symmetry:

$$\mathbf{E}(r,\theta,z) = \mathbf{E}(r)\exp\Big(jL\theta + jk_0 n_{\text{eff}} z - j\omega t\Big)$$
$$\mathbf{H}(r,\theta,z) = \mathbf{H}(r)\exp\Big(jL\theta + jk_0 n_{\text{eff}} z - j\omega t\Big) \quad (1)$$

where $\mathbf{E}$ includes the three cylindrical components of the electric field and $\mathbf{H}$, of the magnetic field; k_0 is the vacuum wavenumber $2\pi/\lambda$; n_{eff} the effective index of the mode; and L is the integer that determines the azimuthal dependence of the mode in θ. It is worth noting that the core mode has $L = 1$ when dealing with EH modes, unlike for LP modes. More details on the dispersion models of the materials and how the modes are calculated are shown in Ref. [35].

To find the cladding modes that can be excited by the LPG, we found the crossings between the cladding mode dispersion curves, and the phase matching condition, which is given by the period of the LPG, designated as Λ:

$$\lambda_{\text{peak}} = (n_{\text{eff}}^{(\text{core})} - n_{\text{eff}}^{(\text{clad})})\Lambda \quad (2)$$

where $n_{\text{eff}}^{(\text{core})}$ is the effective index of the core mode, while $n_{\text{eff}}^{(\text{clad})}$ is the effective index of the cladding mode.

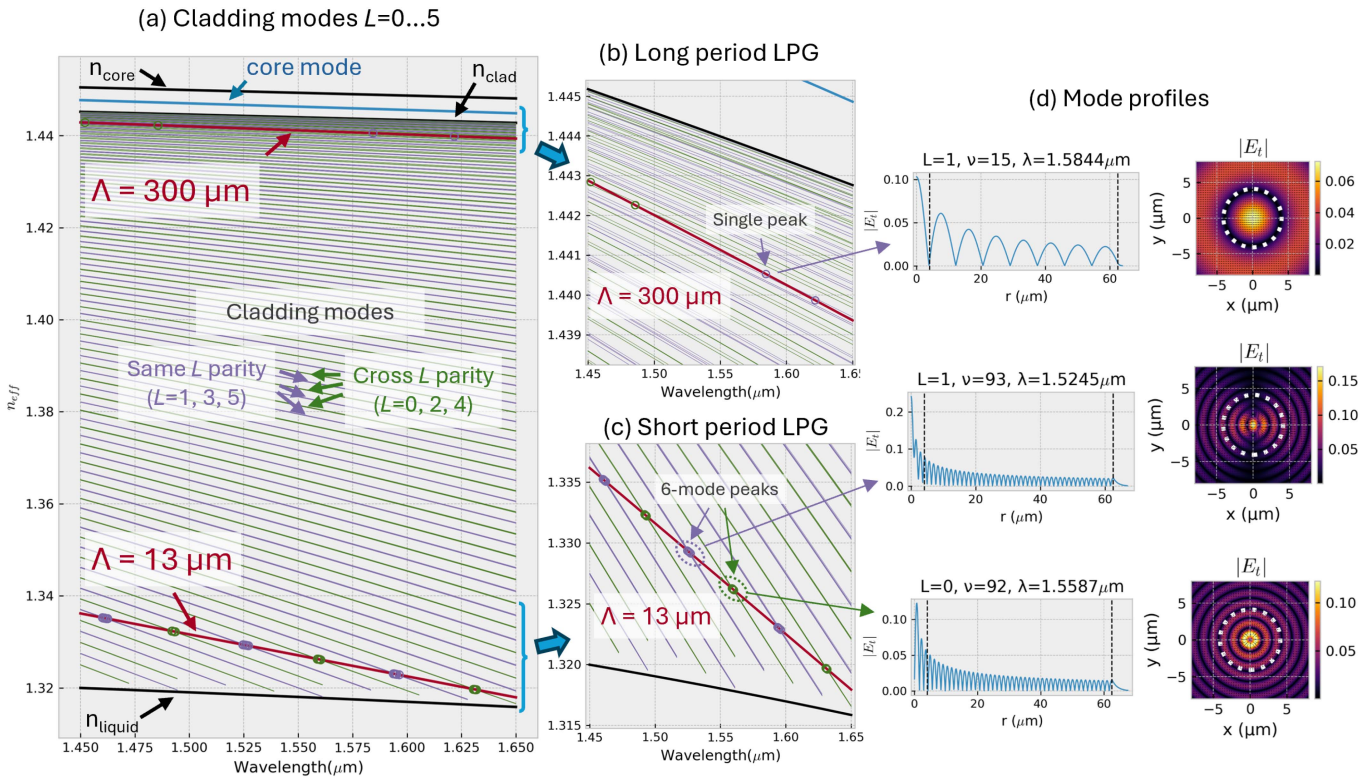

Fig. 2. Calculated cladding mode dispersion curves and mode profiles. (a) Core mode (cyan, L=1) and cladding modes for L between 0 and 5 (odd L, violet, even L, green). Red lines represent the phase matching condition for LPG periods of 300 μm and 13 μm, thus crossings with these lines show the expected LPG peak wavelengths, which are encircled; (b) zoom around 300 μm-period modes; (c) zoom around 13 μm period-modes. Mode clustering by L parity is clearly appreciated for small-period LPGs. (d) Mode profiles of some selected peaks, showing the modulus of the radial profile of the transverse electric field E_t and the 2D plot around the core area. More mode profiles are shown in the Supplementary Material section.

In Fig. 2 we show all cladding modes for L values between 0 and 5. Higher L values are unlikely to be excited as their overlap in the core region becomes very low. We also show the phase matching conditions for a typical LPG with period 300 μm and for a short period equal to 13 μm. It is worth noting the fact that for higher-order cladding modes (with lower effective indices), the modes tend to cluster by L parity, which makes the transmission spectrum as an interleaved set of two kinds of peaks, the ones with odd L values (1, 3, 5), which conserve parity with respect to the core mode, and with even L values (0, 2, 4) where parity is changed by the perturbation. Parity change can occur only if the perturbation is non-symmetrical, which can happen in femtosecond-written LPGs with very small volume of index change which can be slightly off-center. The main advantage of the clustering is that, even though each peak can be a superposition of several modes, the widening of the peak is limited due to the strong clustering of the modes in same-parity families. Our model currently does not predict the precise widths of the experimental transmission dips, as that would require knowing the coupling coefficients to each cladding modes, but it can accurately predict the spectral positions of these peaks.

In Fig. 2(d) we also show the normalized mode profiles of some selected modes from periods of 300 and 13 μm. The feature differences between long and small-period LPGs can be appreciated. The profiles of all the modes in those regions are shown in the supplementary material section, in Fig. S1. We designate each mode with its L number and its order ν, which starts from one and increases in decreasing order of effective index, which is the notation used in Ref. [45]. In Fig. S2 we show a zoomed plot of the profiles of two modes close to the fiber-water interface, to compare the evanescent fields of long-period and small-period LPGs. It is worth noting the much higher evanescent field of the higher-order cladding modes in the liquid with respect to the low-order mode, which is the cause of a higher sensitivity of higher-order modes to liquid index change.

Regarding the sensitivities, we calculated them by simply recomputing the cladding modes after applying a small index change in the liquid. The peak shift divided by the refractive index change provided an accurate value of the sensitivity of each cladding mode. In Fig. 3 we show the sensitivities of all the modes excitable with periods of 13 and 300 μm. The pattern of alternating parities is appreciated, with a common increasing trend in sensitivity with wavelength. Regarding the sensitivity values, the small-period LPGs have positive sensitivities (redshift for increasing liquid refractive index) between 200 and 700 nm/RIU, while the long-period LPGs are negative, and stay below -150 nm/RIU. Regarding the sensitivites to temperature variations, we also estimated them by introducing thermo-optic coefficients to water and silica. The results showed a negative thermal sensitivity (due to water's large negative thermo-optic coefficient), which varies between -10 and -50 pm/K for peaks between 1450 and 1650 nm. These estimations suggest that sensors aiming to detect few-pm spectral shifts should either stabilize the temperature or find methods to compensate the thermal drift by temperature monitoring.

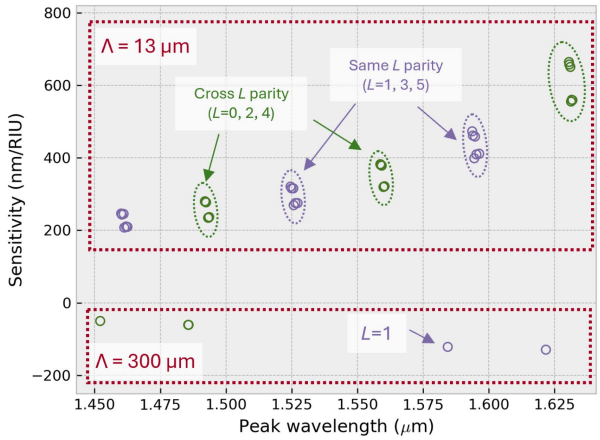

Fig. 3. Sensitivity calculations for each peak wavelength for the two LPG periods, 300 and 13 μm. Circles represent the LPG peak positions for L values between 0 and 5, where odd L modes are violet and even L modes are green. It is worth noting the sign difference between short and long-period LPGs, and the increasing trend of sensitivity with increasing wavelength.

To better understand the dependence of sensitivities of each mode, one can also use the analytical equation from the the group indices of core and cladding modes [46]:

$$S_{liq} = \frac{d\lambda}{dn_{liq}} = \frac{\lambda}{n_g^{(core)} - n_g^{(clad)}} \frac{\partial n_{eff}^{(clad)}}{\partial n_{liq}} \tag{3}$$

where S_{liq} is the sensitivity to liquid index variations, n_{liq} is the refractive index of the liquid, and $n_g^{(core)}$ and $n_g^{(clad)}$ are the group indices of the core and cladding modes respectively. The partial derivative term is proportional to the evanescent field in the liquid, while the difference between the group indices contain the dispersion mismatch, which shows that a divergence occurs when both have the same group index. This condition is reached at the so-called turn-around point (TAP) [47], where the sensitivity also changes sign as predicted by the equation.

Another useful analytical equation regards the expected peak width of the LPG cladding mode, assuming critical coupling condition [46]:

$$\Delta\lambda \approx \frac{0.8\lambda^2}{L(n_g^{(core)} - n_g^{(clad)})} \tag{4}$$

where $\Delta\lambda$ is the full-width half-maximum of the peak and L is the length of the LPG under critical coupling condition. In Fig. 4, we evaluate and plot (3) and (4) to gain further insight into the sensitivity and peak linewidth across different operating regimes. The plot includes all cladding modes with azimuthal order L between 0 and 5 for a standard single-mode fiber immersed in water at a wavelength of 1.55 μm. It is worth noting that the apparent enhancement in wavelength sensitivity near the turn-around point, corresponding to a grating period of approximately 200 μm, vanishes when the sensitivity is normalized to the corresponding peak linewidth. This is the reason why some authors claim that there is no benefit in working at the turn-around point in terms of sensing overall performance [48]. On the other hand, in small-periods LPGs, the sensitivity enhancement is not coupled with linewidth broadening, which

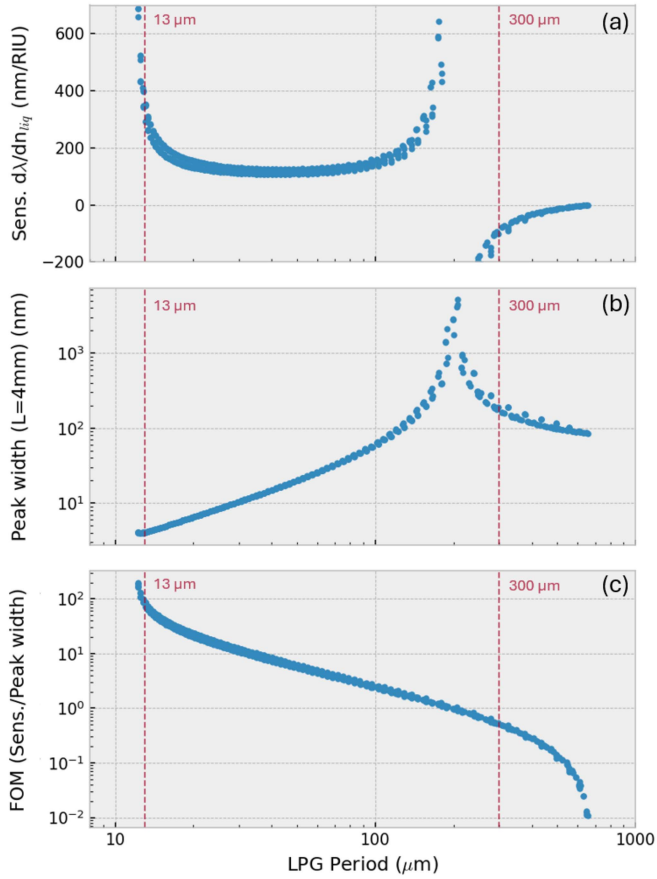

Fig. 4. Sensitivities and peak widths of all the cladding modes of a standard single-mode fiber in water having L values between 0 and 5, at wavelength λ=1.55 μm calculated with the analytical equations for different LPG periods. (a) Sensitivities; (b) Peak FWHM for an LPG length of 4 mm and critical coupling condition; (c) Figure-of-merit (FOM) defined as sensitivity divided by peak width. It is worth noting the turn-around point for periods around 200 μm, which cause a divergence in sensitivity, but when normalizing to the peak width the enhancement vanishes. On the other hand, in the small-period region of the plot, both the sensitivity and the FOM increase, as the enhancement is caused by the higher evanescent field and not by the dispersion matching. It is also worth noting that the trends do not strongly depend of the L value, which means that families of peaks are expected to shift with similar responsivities.

means that a better sensing performance can be expected from these devices.

Finally, regarding the expected difference between LPGs in transmission mode and in reflection mode, we predict the behavior to be very similar in both cases. The reason is because the reflective coating reflects all the signal, which enables a second pass in the opposite direction. However, the system does not behave like a grating of twice the length, nor like an interferometer, because the cladding modes excited through the first pass are lost in the segment between the LPG and the mirror, as the metal is also deposited along its lateral surface. Therefore we expect the reflection spectrum to be the result of a double-pass transmission, which should follow this equation:

$$R_{LPG}(\lambda) = T_{LPG}^2(\lambda) \tag{5}$$

where R_{LPG} designates the reflection spectrum in reflection mode (with a mirror in the end), and T_{LPG} is the single-pass transmission of the LPG. We assumed the reflectivity of the

mirror to be 100%, and the mirror to be close enough to the LPG to neglect any polarization drift between the LPG and the mirror. Finally, any reflection feature of the actual LPG was also assumed to be much weaker than the background signal being reflected. With these assumptions, the peaks in reflection mode are expected to have a similar profile, but with twice the depth with respect to the single-pass transmission mode.

III. Experimental Section

A. SP-LPG Fabrication Setup

In this study, SP-LPGs are fabricated on standard single-mode fibers (SMF-28). The gratings are inscribed using a femtosecond laser (Spectra Physics Spirit One 1040 8 SHG), operating at a wavelength of 520 nm, on a short section of the fiber that has been mechanically stripped and cleaned with isopropyl alcohol (IPA). Prior to the writing process, the stripped fiber segment is placed on a glass slide and immersed in index-matching liquid (Cargille Laboratories). A cover slip is then placed over the fiber to minimize focal distortion or lensing effects arising from the fiber's curved surface. The entire assembly, including the stripped SMF, is mounted on a computer-controlled 3D translation stage (Newport M-37 series).

During the LPG fabrication, the stage translates along the fiber axis at a constant speed of 99.913 μm/s, while the laser is modulated using an external function generator (Agilent 33250A) producing a square wave with a 50% duty cycle. This modulation enables inscription of the grating with the desired period Λ into the fiber core. The laser has a repetition rate of 200 kHz and a pulse duration of approximately 350 fs, attenuated to an average power of 3.5 mW. The laser pulses are focused onto the fiber using a 40$\times$ objective (ZEISS EC Plan-Neofluar 40$\times$, NA 0.75). The optimum laser power for 4-mm-long LPGs was found by varying it until the transmission dips showed maximum contrast.

After the manufacturing process, the SMF with the inscribed LPG is removed from the stage and cleaned with IPA to eliminate any residual index-matching liquid before recording the transmission spectrum. This process is performed to fabricate SP-LPGs with period lengths of 13 μm as that shown in Fig. 5

The reproducibility of the SP-LPG fabrication process was assessed in our earlier work [35] by analyzing the transmission spectra of multiple SP-LPGs fabricated on different days using the same inscription protocol. The spectra acquired in air exhibit consistent resonance patterns, with the wavelength separation between consecutive resonant dips (Free Spectral Range, FSR) remaining constant across samples. This consistency confirms the high reproducibility of the fabrication process and the stability of the grating parameters, ensuring reliable device performance across different fabrication batches.

The fabricated fiber optic device can be operated in reflection mode by applying reflective paint to the fiber end. To do this, we first cleaved the fiber end at a 90° angle, approximately 2–3 cm from the grating, using a mechanical cleaver. The cleaved end is then cleaned with IPA and coated with a commercial reflective paint (Cadence, mirror-effect paint) [49]. As shown in Fig. 6 a and d, the fabrication of the reflection-type SP-LPG does not alter the peak position but leads to an increase in peak depth and a reduction in overall transmitted intensity.

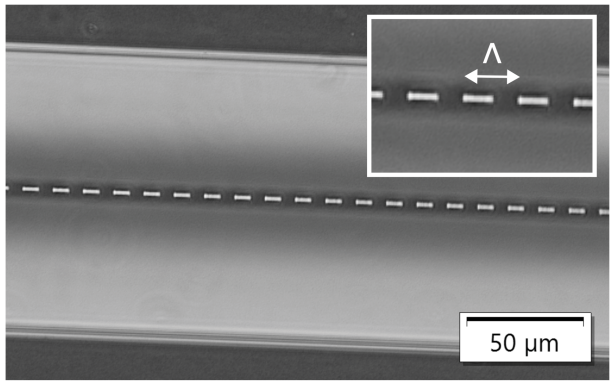

Fig. 5. Phase contrast microscopy image of an SP-LPG. The dashed lines in the fiber core indicate regions exposed to femtosecond laser pulses. The inset shows a magnified view of the fiber core, highlighting the grating period (Λ) of 13 μm.

B. Materials and Chemicals

Polydimethylsiloxane (PDMS) (SYLGARD^{TM} 184 Silicone Elastomer Kit) was purchased from Dow Corning. Double-coated adhesive acrylic tape (NITTO, 5000ND) was obtained from NITTO, Italy. Glycerol (Sigma-Aldrich, G7757), isopropanol (IPA, RS Italy, 187-6955), and deionized water (DI water) were used for refractive index (RI) sensitivity measurements and sample preparation.

To determine the RI of the glycerol–water mixtures used in this study, we adopted a third-degree polynomial model, following the approach proposed by Saunders et al. [50]. The RI of the solution (n_{sol}) was calculated as a function of the glycerol weight fraction (w) using the equation:

$$n_{\text{sol}} = Aw^3 + Bw^2 + Cw + D \tag{6}$$

where the coefficients are $A = -0.0215$, $B = -0.0512$, $C = 0.111$, and $D = 1.318$, the latter corresponding to the RI of pure water at 1550 nm. Since the RI of glycerol–water mixtures exhibits a predictable spectral dependence, the model was extended to other wavelength ranges by adjusting the coefficient D as an offset, using reference values from [51]. This approach ensures accurate RI estimation across the relevant spectral region. To validate the glycerol content in each solution, the RI was cross-checked using a refractometer (DBR 95 Digital Refractometer) operating in the visible range.

C. Optomicrofluidic Chip and Interrogation Platform

Schematics of the chip assembly and a photograph of the optomicrofluidic platform are provided in the Supplementary Material (Fig. S3). The SP-LPGs inscribed on the optical fiber (III in Fig. S3a) are positioned on a standard glass slide (IV in Fig. S3a) and bonded to a 3 mm thick polydimethylsiloxane (PDMS) slab (I in Fig. S3a) using a 350 μm thick double-coated adhesive acrylic tape (NITTO, 5000ND, II in Fig. S3a). The tape is cut into 3 cm $\times$ 2 cm sections using a scalpel, which is also used

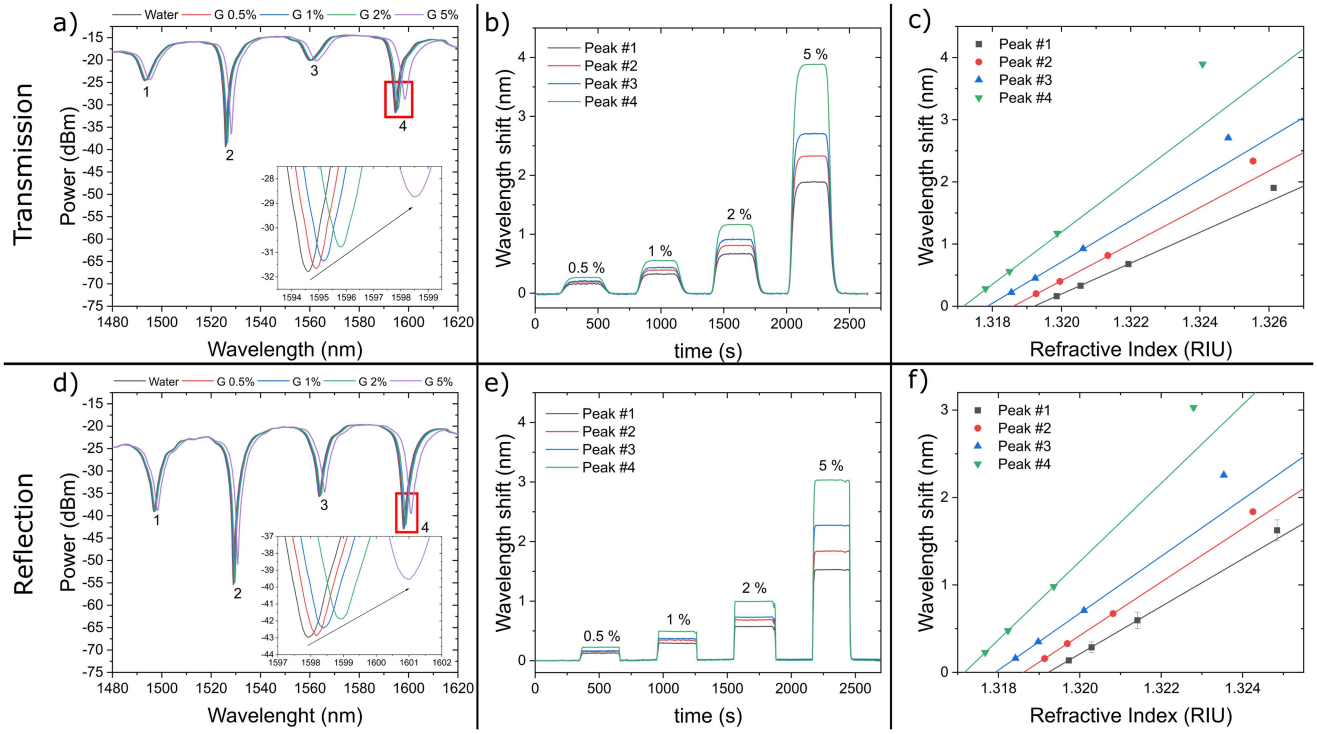

Fig. 6. Transmission (a, b, c) and reflection (d, e, f) characterization of SP-LPGs exposed to aqueous solutions with different RI, prepared using water/glycerol mixtures with concentrations from 0.5% to 5% v/v. Panels (a) and (d) show the transmission and reflection spectra, respectively, with the insets presenting zoomed-in views of the most sensitive peaks (i.e., right-most), where the black arrows indicate the red shift of the resonance as the RI increases. Panels (b) and (e) display the corresponding sensorgrams, showing the shift in the resonance peak upon exposure to glycerol solutions at varying concentrations (v/v). After each incubation, the microfluidic chip was flushed with DI water, restoring the peak to its initial position. The peak shifts for SP-LPGs operating in transmission (c) and reflection (f) modes are plotted against the refractive index of the corresponding water/glycerol mixtures. Both configurations exhibit a linear response to RI changes up to 2% glycerol, with sensitivities determined by linear regression (solid lines) within this range. Each data point represents the average of triplicate experiments, with error bars denoting the standard deviation.

to carve out an S-shaped channel in the middle of the tape, forming the microfluidic path. The main (long) section of the channel is approximately 1.5 cm long and 1.5 mm wide, designed to accommodate the SP-LPGs. Two shorter side arms, each about 6.5 mm in length, connect the main channel to the inlet and outlet ports. The only critical requirement in this assembly is to ensure that the double-sided tape has a thickness greater than the optical fiber diameter (125 μm) to prevent compression. For the device operating in reflection mode, the SP-LPG is confined within the microfluidic channel, while the fiber end with the reflective coating extends beyond the PDMS slab and remains isolated from the flowing fluid. The PDMS slab dimensions (I in Fig. S3a) are 3 cm $\times$ 2 cm $\times$ 3 mm (length $\times$ width $\times$ height), and 2.5 mm diameter holes are punched into it to allow sample delivery through 0.7 mm inner diameter Tygon tubing. The complete chip assembly is illustrated schematically in Fig. S3b and shown in a photograph in Fig. S3c.

The assembled chip is then mounted in the sensing setup described in Fig. 1. The major difference between the two sensing configurations is that operation in reflection mode necessitated the inclusion of an optical circulator to separate the forward-propagating input signal from the backward-reflected signal, allowing proper acquisition of the reflected spectrum separating by polarization.

The experiments are performed by flowing aqueous samples (i.e., DI water and glycerol solutions with volume concentrations ranging from 0.5% to 5%) into the microfluidic chip using a single syringe pump (NE-1000, New Era Pump Systems, Inc.) operating at a flow rate of 100 μL/min. Transmission and reflection spectra are recorded using an optical interrogator (Luna Technologies Hyperion si155) with a sampling rate of 100 Hz.

The manufacturer's interrogator software (ENLIGHT 1.18.8.0) is used to monitor real-time variations in the transmission spectra and track peak shifts.

IV. Results and Discussion

To evaluate the RI sensitivity of the SP-LPGs, the gratings are exposed to aqueous solutions with varying RI values, specifically water and water–glycerol mixtures with concentrations ranging from 0.5% to 5% v/v [50]. This is accomplished by positioning the section of the optical fiber containing the grating within a microfluidic chip, as illustrated in Fig. S3. After integrating the chip with the remaining microfluidic components and aligning the fiber within the optical interrogation setup (Fig. 1), the SP-LPG is first exposed to DI water, which serves as the reference condition for subsequent measurements.

The Fig. 6(a) and (d) show the full transmission spectra of the 13 μm SP-LPGs operating in transmission and reflection modes, while the insets provide a magnified view of the rightmost peak for each configuration. Initially, DI water is flowed through the microfluidic chip for approximately 300 s to establish the

TABLE I
RI SENSITIVITY OF THE TWO TYPES OF SP-LPGS, COMPARED WITH VALUES OBTAINED FROM THEORETICAL SIMULATIONS. THE SIMULATED SENSITIVITIES ARE REPORTED AS THE LOWER AND UPPER BOUNDS FOR ALL CLADDING MODES IN THE FAMILY WITH AZIMUTHAL MODE NUMBER L RANGING FROM 0 TO 5 (AS SHOWN IN FIG. 3), WHILE THE EXPERIMENTAL VALUES ARE DERIVED FROM LINEAR REGRESSION OF THE SHIFTS SHOWN IN FIG. 6 C AND D.

Peak #	Theoretical Sensitivity (nm/RIU)	Experimental Sensitivity (nm/RIU) Transmission	Experimental Sensitivity (nm/RIU) Reflection
1	235 - 279	248 ± 2.1	271 ± 1.9
2	270 - 322	294 ± 3.7	305 ± 0.4
3	319 - 385	332 ± 3.7	326 ± 5.0
4	400 - 475	421 ± 11.0	448 ± 0.4

baseline, after which the first glycerol solution (0.5% v/v) is introduced and maintained for an additional 300 s. Upon contact with the grating, the increase in the surrounding medium's RI induces a red shift in the SP-LPG's transmission peaks. This shift is clearly observed in the insets of Fig. 6(a) and (d), and is further quantified over time in Fig. 6(b) and (e), which show the wavelength shift of each SP-LPG peak for both configurations.

Following each glycerol exposure, the system is flushed with DI water to restore the spectra to their initial state. This measurement cycle is repeated using four glycerol concentrations (0.5, 1, 2, and 5% v/v), yielding the spectral responses and sensorgrams shown in Fig. 6.

The measured peak shifts are used to determine the RI sensitivity of the SP-LPGs. The wavelength shifts induced by exposure to the various water–glycerol mixtures are plotted as a function of RI in Fig. 6(c) and (f). As shown, both configurations exhibit a nonlinear response at 5% glycerol concentration. This behavior is predicted from the simulations and previously reported in the literature [32], and is attributed to a gradual transition from cladding modes to lossy modes, which also causes a reduction of peak contrast and broadening of the resonance. Since both SP-LPG configurations demonstrate a linear relationship between peak shift and RI up to 2% glycerol, RI sensitivities are extracted by performing linear regression within this range, as shown in Fig. 6(c) and (f).

Finally, the experimental sensitivity values obtained are reported in Table I, alongside theoretical predictions from Fig. 3. The range given for the simulated values regards the maximum and minimum sensitivity predicted within all the cladding modes belonging to the same peak family. Regarding the experimental data, we show the measured sensitivities for each peak and for each experimental configuration (transmission and reflection mode). The experimental uncertainties are the ones obtained from the linear regression of the fit. The data shows very similar sensitivity values for both experimental modes, and a very good fit with the theoretical predictions.

It is important to notice that SP-LPG sensors, like other fiber grating-based devices, can exhibit cross-sensitivity to temperature, strain, and mechanical deformation. Several strategies can be implemented to minimize these effects. One approach exploits the grating's reflection spectrum, using the Bragg reflection to monitor temperature and strain variations and apply compensation routines during data analysis [33]. Alternatively, a FBG can be inscribed in close proximity to the SP-LPG in a cascaded configuration, enabling simultaneous detection of thermal, mechanical, and optical parameters [52]. A simpler and more flexible strategy could involve the integration of two distinct fiber sensors within the same microfluidic platform, allowing real-time correction for temperature or mechanical effects. Future work will focus on systematically investigating these approaches to enhance the accuracy and robustness of the SP-LPG-based sensing platform for real-world applications.

V. CONCLUSION

In this study, we compared the performance of SP-LPGs operating in transmission and reflection modes for RI sensing. While both configurations demonstrated comparable sensitivity and resolution, reflection-mode operation enables single-ended sensing, which is advantageous in applications where access to both fiber ends is restricted. This added flexibility comes with minimal impact on sensing performance, as the spectral features and RI response were consistent with those observed in transmission mode and aligned with theoretical predictions. Importantly, the ability to operate in reflection mode without compromising sensitivity expands the integration potential of SP-LPGs in compact and minimally invasive sensing platforms, such as biomedical catheters, embedded probes or environmental remote sensors. Future efforts will focus on extending this approach to functionalized SP-LPGs for selective biosensing applications and exploring compensation strategies for cross-sensitivity to temperature and strain.

ACKNOWLEDGMENT

The authors wish to thank Mikel Bravo from Public University of Navarra, Spain, for help with the deposition of the reflective mirror.

REFERENCES

[1] F. Baldini, M. Brenci, F. Chiavaioli, A. Giannetti, and C. Trono, "Optical fibre gratings as tools for chemical and biochemical sensing," *Anal. Bioanalytical Chem.*, vol. 402, pp. 109–116, 2012.
[2] F. Chiavaioli, F. Baldini, S. Tombelli, C. Trono, and A. Giannetti, "Biosensing with optical fiber gratings," *Nanophotonics*, vol. 6, no. 4, pp. 663–679, 2017.
[3] X. Zhang et al., "A novel structure of microfiber-based sensor for on-site/insitu detection of heavy metal ions," presented at Conf. Lasers Electro-Optics/Pacific Rim, Hong Kong, SAR, China, Jul. 29–Aug. 03, 2018, Paper Th3L–1.
[4] R. Rohan, K. Venkadeshwaran, and P. Ranjan, "Recent advancements of fiber Bragg grating sensors in biomedical application: A review," *J. Opt.*, vol. 53, no. 1, pp. 282–293, 2024.
[5] A. D. Kersey et al., "Fiber grating sensors," *J. Lightw. Technol.*, vol. 15, no. 8, pp. 1442–1463, 1997.
[6] V. Bhatia, "Properties and sensing applications of long-period gratings," Ph.D. dissertation, Virginia Polytech. Inst. State Univ., 1996.
[7] J. Ran et al., "Mechanically induced long-period fiber gratings and applications," *Photonics*, vol. 11, no. 3, 2024, Art. no. 223.
[8] K. Zhou, X. Chen, L. Zhang, and I. Bennion, "Implementation of optical chemsensors based on HF-etched fibre Bragg grating structures," *Meas. Sci. Technol.*, vol. 17, no. 5, 2006, Art. no. 1140.
[9] A. Ruskuc et al., "Excitation of higher-order modes in optofluidic photonic crystal fiber," *Opt. Exp.*, vol. 26, no. 23, pp. 30245–30254, 2018.

[10] W. W. Morey, G. Meltz, and W. H. Glenn, "Fiber optic Bragg grating sensors," *Proc. SPIE*, vol. 1169, pp. 98–107, 1990.

[11] F. Esposito, A. Srivastava, L. Sansone, M. Giordano, S. Campopiano, and A. Iadicicco, "Label-free biosensors based on long period fiber gratings: A review," *IEEE Sensors J.*, vol. 21, no. 11, pp. 12692–12705, Jun. 2021.

[12] X. Shu, T. Allsop, B. Gwandu, L. Zhang, and I. Bennion, "High-temperature sensitivity of long-period gratings in B-Ge codoped fiber," *IEEE Photon. Technol. Lett.*, vol. 13, no. 8, pp. 818–820, Aug. 2001.

[13] Y. Zhang et al., "Sensing characteristics of long period grating by writing directly in SMF-28 based on 800 nm femtosecond laser pulses," *Opt. Laser Technol.*, vol. 121, 2020, Art. no. 105839.

[14] I. Del Villar, O. Fuentes, F. Chiavaioli, J. M. Corres, and I. R. Matias, "Optimized strain long-period fiber grating (LPFG) sensors operating at the dispersion turning point," *J. Lightw. Technol.*, vol. 36, no. 11, pp. 2240–2247, Jun. 2018.

[15] S. K. A. K. Bey, T. Sun, and K. T. Grattan, "Simultaneous measurement of temperature and strain with long period grating pairs using low resolution detection," *Sensors Actuators A: Phys.*, vol. 144, no. 1, pp. 83–89, 2008.

[16] T. Allsop et al., "Bending characteristics of fiber long-period gratings with cladding index modified by femtosecond laser," *J. Lightw. Technol.*, vol. 24, no. 8, pp. 3147–3154, Aug. 2006.

[17] K. Ren, L. Ren, J. Liang, X. Kong, H. Ju, and Z. Wu, "Highly strain and bending sensitive microtapered long-period fiber gratings," *IEEE Photon. Technol. Lett.*, vol. 29, no. 13, pp. 1085–1088, Jul. 2017.

[18] R. Subramanian, C. Zhu, H. Zhao, and H. Li, "Torsion, strain, and temperature sensor based on helical long-period fiber gratings," *IEEE Photon. Technol. Lett.*, vol. 30, no. 4, pp. 327–330, Feb. 2018.

[19] X. Shu, L. Zhang, and I. Bennion, "Sensitivity characteristics of long-period fiber gratings," *J. Lightw. Technol.*, vol. 20, no. 2, pp. 255–266, Feb. 2002.

[20] F. Esposito, "Chemical sensors based on long period fiber gratings: A review," *Results Opt.*, vol. 5, 2021, Art. no. 100196.

[21] L. Chen et al., "High-sensitive refractive index sensor based on the long-period gratings inscribed in the tapered fiber at dispersion turning point," *Opt. Commun.*, vol. 569, 2024, Art. no. 130798.

[22] Y. Zhuo, P. Ma, P. Jiao, and X. Yuan, "Application of long-period fiber grating sensors in structural health monitoring: A review," *CivilEng*, vol. 5, no. 3, pp. 559–575, 2024.

[23] A. Stăncălie et al., "Long period gratings in unconventional fibers for possible use as radiation dosimeter in high-dose applications," *Sensors Actuators A: Phys.*, vol. 271, pp. 223–229, 2018.

[24] S. Korposh, R. Selyanchyn, S. James, R. Tatam, and S.-W. Lee, "Identification and quality assessment of beverages using a long period grating fibre-optic sensor modified with a mesoporous thin film," *Sens. Bio-Sens. Res.*, vol. 1, pp. 26–33, 2014.

[25] G. Quero et al., "Long period fiber grating working in reflection mode as valuable biosensing platform for the detection of drug resistant bacteria," *Sensors Actuators B: Chem.*, vol. 230, pp. 510–520, 2016.

[26] C. Trono, "Long period fiber grating-based biosensing: Recent trends and future perspectives," *TrAC Trends Anal. Chem.*, vol. 179, 2024, Art. no. 117875.

[27] X.-W. Zhao and Q. Wang, "Mini review: Recent advances in long period fiber grating biological and chemical sensors," *Instrum. Sci. Technol.*, vol. 47, no. 2, pp. 140–169, 2019.

[28] M. Peng et al., "Femtosecond laser direct writing of long period fiber grating sensor with high refractive index sensitivity," *Opt. Fiber Technol.*, vol. 81, 2023, Art. no. 103511.

[29] W. Bu, X. Wang, Z. Wu, J. Lin, P. P. Shum, and J. Pu, "Temperature-insensitive refractive index sensor based on high-order-resonance short-line long-period fiber grating," *Sensors Actuators A: Phys.*, vol. 360, 2023, Art. no. 114540.

[30] Z.-M. Zheng, Y.-S. Yu, X.-Y. Zhang, Q. Guo, and H.-B. Sun, "Femtosecond laser inscribed small-period long-period fiber gratings with dual-parameter sensing," *IEEE Sensors J.*, vol. 18, no. 3, pp. 1100–1103, Feb. 2018.

[31] J. Wang et al., "Line by line inscribed small period long period grating for wide range refractive index sensing," *Opt. Commun.*, vol. 508, 2022, Art. no. 127821.

[32] F. Shen, C. Wang, Z. Sun, K. Zhou, L. Zhang, and X. Shu, "Small-period long-period fiber grating with improved refractive index sensitivity and dual-parameter sensing ability," *Opt. Lett.*, vol. 42, no. 2, pp. 199–202, 2017.

[33] J. Cai et al., "A small-period long-period fiber grating biosensor based on immobilization of concanavalin a on polydopamine nanospheres for simultaneous detection of D-glucose and temperature," *Measurement*, vol. 242, 2025, Art. no. 115877.

[34] R. Zhao, H. Liu, and X. Shu, "Femtosecond laser-inscribed off-axis high-order mode long-period grating for independent sensing of curvature and temperature," *Opt. Exp.*, vol. 30, no. 21, pp. 37697–37710, 2022.

[35] R. Funari, R. M. A. Ayaz, F. Di Pasquale, and C. J. Oton, "Design and fabrication of short-period long period gratings for refractive index sensing," *Opt. Exp.*, vol. 33, no. 14, pp. 29786–29801, 2025.

[36] A. Iadicicco, A. Cusano, S. Campopiano, A. Cutolo, and M. Giordano, "Thinned fiber Bragg gratings as refractive index sensors," *IEEE Sensors J.*, vol. 5, no. 6, pp. 1288–1295, Dec. 2005.

[37] V. Ahsani, F. Ahmed, M. B. Jun, and C. Bradley, "Tapered fiber-optic mach-Zehnder interferometer for ultra-high sensitivity measurement of refractive index," *Sensors*, vol. 19, no. 7, 2019, Art. no. 1652.

[38] D. Capelli, V. Scognamiglio, and R. Montanari, "Surface plasmon resonance technology: Recent advances, applications and experimental cases," *TrAC Trends Anal. Chem.*, vol. 163, 2023, Art. no. 117079.

[39] P. P. A. Suthanthiraraj and A. K. Sen, "Localized surface plasmon resonance (LSPR) biosensor based on thermally annealed silver nanostructures with on-chip blood-plasma separation for the detection of dengue non-structural protein NS1 antigen," *Biosensors Bioelectron.*, vol. 132, pp. 38–46, 2019.

[40] R. Funari, K.-Y. Chu, and A. Q. Shen, "Multiplexed opto-microfluidic biosensing: Advanced platform for prostate cancer detection," *ACS Sensors*, vol. 9, no. 5, pp. 2596–2604, 2024.

[41] S. Z. Ahmed, M. Hasan, K. Kim, and S. Kim, "Zero-crosstalk silicon photonic refractive index sensor with subwavelength gratings," *Nano Convergence*, vol. 11, no. 1, 2024, Art. no. 39.

[42] X. Ou et al., "Microring resonator based on polarization multiplexing for simultaneous sensing of refractive index and temperature on silicon platform," *Opt. Exp.*, vol. 30, no. 14, pp. 25627–25637, 2022.

[43] C. Yeh and G. Lindgren, "Computing the propagation characteristics of radially stratified fibers: An efficient method," *Appl. Opt.*, vol. 16, no. 2, pp. 483–493, 1977.

[44] S. R. Dods, "Fiber vector modesolver-improvements to the efficient 4×4 matrix method," presented at Integrated Photonics Research and Applications, Uncasville, CT, USA, Apr. 24–26, 2006, Paper ITu F5.

[45] T. Erdogan, "Cladding-mode resonances in short-and long-period fiber grating filters," *JOSA A*, vol. 14, no. 8, pp. 1760–1773, 1997.

[46] C. Deleau, H. C. Seat, O. Bernal, and F. Surre, "High-sensitivity integrated sin rib-waveguide long period grating refractometer," *Photon. Res.*, vol. 10, no. 2, pp. 564–573, 2022.

[47] P. Biswas, N. Basumallick, S. Bandyopadhyay, K. Dasgupta, A. Ghosh, and S. Bandyopadhyay, "Sensitivity enhancement of turn-around-point long period gratings by tuning initial coupling condition," *IEEE Sensors J.*, vol. 15, no. 2, pp. 1240–1245, Feb. 2015.

[48] R. M. Carter et al., "Experimental difficulties with LPG sensors operating close to the phase turning points," *J. Lightw. Technol.*, vol. 34, no. 17, pp. 3999–4004, Sep. 2016. [Online]. Available: https://opg.optica.org/jlt/abstract.cfm?URI=jlt-34-17-3999

[49] I. Jaso, E. Mejia-Olivo, M. Bravo, D. Leandro, and M. L.-A. Sainz, "Fiber optic mirror fabrication using general-purpose metallic pigments," *Proc. SPIE*, vol. 12643, 2023, Art. no. 1264330.

[50] J. E. Saunders, C. Sanders, H. Chen, and H.-P. Loock, "Refractive indices of common solvents and solutions at 1550 nm," *Appl. Opt.*, vol. 55, no. 4, pp. 947–953, 2016.

[51] G. M. Hale and M. R. Querry, "Optical constants of water in the 200-nm to 200-μm wavelength region," *Appl. Opt.*, vol. 12, no. 3, pp. 555–563, Mar. 1973. [Online]. Available: https://opg.optica.org/ao/abstract.cfm?URI=ao-12-3-555

[52] Y. Yan, Z. Gu, Y. Wang, and J. Du, "Design and simulation of reflective fiber grating sensor for simultaneous monitoring of CTD in marine environment," *J. Opt.*, 2024, doi: 10.1007/s12596-024-02157-6.